Journal of Physics: Conference Series **75** (2007) 012012 doi:10.1088/1742-6596/75/1/012012

Experimentally observed effects of yaw misalignment on the inflow in the rotor plane

W Haans, GAM van Kuik and GJW van Bussel

Faculty of Aerospace Engineering, Delft University of Technology, Delft, 2629 HS, The Netherlands

E-mail: w.haans@tudelft.nl

Abstract. Near-wake measurements, focussed on yawed flow conditions, are conducted on a wind turbine rotor model in an open jet wind tunnel. Tip vortex center locations and phase-locked average flow velocity distributions are recorded. Experimental conditions at the blade are not measured and hence are estimated from a measurement analysis tool, named inverse vortex wake model. The unknown bound circulation is derived by the vortex wake type method without the need for an airfoil model. The analysis of the effects yawed operating conditions have on the blade flow conditions concentrates on the individual contributions of tip, root, trailed and shed vortices to the inflow in the rotor plane.

1. Introduction

Wind turbine rotor aerodynamics is of a three-dimensional, unsteady nature and is characterized by coupled wake and blade aerodynamics. The rotor loads yield structural displacements that in turn alter the loads, resulting in an aero-elastic system. Today's aero-elastic design codes generally employ the Blade Element Momentum (BEM) theory to model the rotor aerodynamics. Less restrictive rotor aerodynamics models, such as vortex wake models, become increasingly popular, as discussed in a recent review article by Hansen *et. al* [1]

The uncertainties associated with blade load and rotor performance predictions of BEM and vortex wake models are considerable, as is exemplified by the 2001 NREL blind comparison of rotor aerodynamics codes with measurements on a model rotor in the NASA-Ames wind tunnel [2]. Recent review articles [3, 4, 5] acknowledge the need for an improved physical understanding of the rotor aerodynamics in order to reduce the modeling uncertainties of today's aero-elastic design codes.

Wind tunnel studies on model rotors aid to an increased insight into rotor aerodynamics. Because of coupled blade and wake aerodynamics, the combined recording of blade loads and the rotor wake is desired. The MEXICO measurements REF X are pivotal in this respect, since both blade loads and the rotor wake, also in the rotor plane, are recorded in detail. In general however, measurements either focus on blade loads or on the rotor wake; the overall picture remains obscured. For a recent overview of near-wake experiments, see Vermeer *et. al* [6].

In order to obtain more information from rotor measurements than is available from the data directly, dedicated measurement analysis tools are constructed. Aerodynamic variables derived are the angle of attack α and, for rotor wake measurements, the blade loads.

Determining the angle of attack
BEM and vortex wake methods utilize airfoil models to determine the blade forces for a given velocity distribution in the rotor plane. The airfoil models require a two-dimensional α. For a two-dimensional airfoil, α is defined by the angle between the undisturbed flow and the airfoil chord. On a rotating blade however, the flow passing a blade section is bent due to the blade rotation, bound circulation induces local velocities and three-dimensional effects are introduced by wake vortices. Hence α is difficult to define and cannot be measured directly.

When both blade loads and the rotor wake velocity at least a single point near the blade are recorded, a combined load-velocity method by Shen *et al.*[7] could be applied to estimate α. Using the recorded loads only, e.g. Van Rooij *et al.*[8] propose a blade pressure method. Vortex wake lifting line methods are employed by Tangler [9] and Sant *et. al* [10] in the prescribed and free wake formulation, respectively. The local rotor load and α combined yield airfoil lift and drag characteristics on the rotating blade, to be used in e.g. BEM and vortex wake models.

For measurements of the rotor wake only, methods to determine α include an azimuthal averaged axial velocity method by Hansen *et al.* [11] and a blade passage phase-locked average axial velocity method by Haans *et. al* [12].

Determining the angle of attack and blade loads
The conditions at the rotor blade are not directly measured for rotor wake experiments. The blade loads and the corresponding α can be derived using methods based on inviscid, incompressible vortex theory; the flow velocity at any point in a domain can be expressed as the vectorial summation of flow velocity induced by all circulation in the domain, found through the Biot-Savart law, and a uniform flow velocity.

An analysis tool by Vermeer and Van Bussel [13] approximates the strength of the bound circulation on the blade for axial flow conditions. The measured velocity is assumed to only have induced velocity contributions from the bound circulation, with the blade represented by a two-dimensional translating line vortex. The Biot-Savart equation is solved for the bound circulation strength. Vermeer [14] subsequently incorporates three-dimensional effects to the model; the blades have finite length, bound circulation is allowed to vary in spanwise direction and the blades rotate. Wake circulation effects are however not included.

Conservation of circulation is applied in an analysis model by Mast *et. al* [15], the induced velocity contains both bound and trailed circulation contributions. The vortex wake geometry is reconstructed from measurements. The bound circulation distribution is represented by a Legendre polynomial function series. The method is referred to as the 'inverse vortex wake method', since the complete blade-wake vortex system is considered, where the term 'inverse' indicates that the model is used as a measurement analysis tool, instead of a prediction tool. Although mathematically elegant, the shapes of the selected Legendre polynomials are not ideally suited to represent the bound circulation distribution, making the model less computationally efficient. Furthermore, the model is only applied to axial flow conditions.

The inverse vortex wake model of Haans *et al.* [16] is numerically discretized in order to increase its flexibility and computational efficiency. Furthermore, its capabilities are extended to yawed flow conditions.

The current paper presents an updated version of the inverse vortex wake method discussed in [16]. Furthermore, blade loads and inflow conditions at the rotor plane are discussed that result from application of the analysis tool to near-wake measurements on a model rotor subject to yawed flow conditions. The objective is to identify main phenomena governing the experimental inflow in yaw.

2. Near-wake measurements

An extensive measurement campaign conducted at the TUDelft focusses on the near-wake of a model rotor in yawed flow conditions, including baseline axial flow conditions. For a detailed discussion on measurement techniques and experimental results, see articles on tip vortex geometry measurements with quantitative smoke visualization [17], on phase-locked velocity measurements with Constant Temperature Anemometry CTA [12, 18] and on dynamic stall observations with both tufts and CTA [19]. Here, the setup, operating conditions and the experimental output are introduced briefly as knowledge hereof helps to understand the discussion on the inverse vortex wake model.

2.1. Experimental Setup and Conditions

The near-wake of a rotor model is measured in an open jet wind tunnel. A schematic of the model rotor setup can be seen in Figure 1. Characteristics of the model rotor are found in Table 1. Set wind tunnel speed W_{jet} is expressed in the cartesian wind tunnel coordinate system $(x_{jet}, y_{jet}$. Aligned with the non-rotating model rotor are a cartesian (x_m, y_m, z_m)- and cylindrical (r, θ, z)-coordinate system. The z- and z_m-axes are equivalent. The origins of both coordinate systems are located in the rotor hub center, with the rotor plane given by $z, z_m = 0$. The blades rotate clockwise, when observing the rotor from an upwind position, with θ_b the blade azimuth angle and Ω the rotational frequency. Ψ is the yaw angle, with y_m the yaw axis.

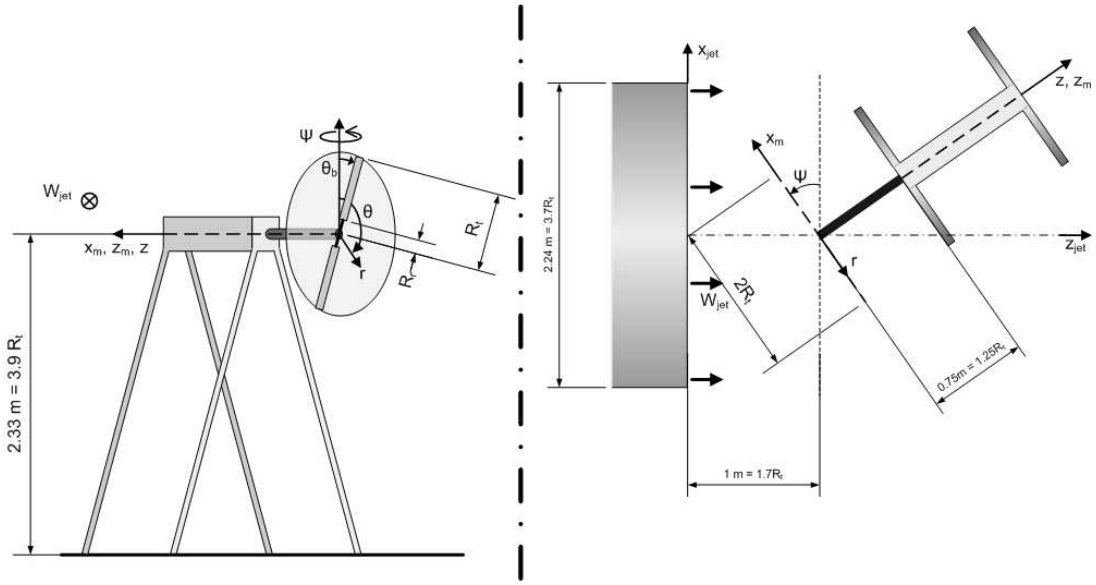

Figure 1. Schematic of the model rotor setup in the open jet wind tunnel. Left plot: front view, looking in downwind direction, right plot: top view.

Three operating conditions are analyzed with the inverse vortex wake model. Wind tunnel wall effects are accounted for by correcting W_{jet} to an equivalent unbounded wind speed W_0^* [12]. For all three conditions, Ω and the tip pitch angle $\theta_{c_{tip}}$ are set to $73.32\,rad/s$ and 2°, respectively. The tip speed ratio corrected for wind tunnel wall effects λ^* for all three conditions is approximately 8, with

$$\lambda^* = \frac{\Omega R_t}{W_0^*}, \tag{1}$$

where R_t is the rotor tip radius. For a point fixed to a rotating blade at $r/R_t = 0.7$, the chord Reynolds number $Re^*_{0.7R}$, turbulence intensity $Tu^*_{0.7R}$ and reduced frequency $k^*_{0.7R}$, all corrected

Number of blades	2
Airfoil section	NACA0012
Rotor tip radius R_t	0.6 m
Rotor root radius R_r	0.18 m
Chord c	0.08 m (constant)
Tip pitch angle $\theta_{c_{tip}}$	experimenter input
Blade pitch angle	$\theta_c(r/R_t) = (6 + \theta_{c_{tip}}) - 6.67 \cdot r/R_t \quad 0.3 \leq r/R_t \leq 0.9$ $\theta_c(r/R_t) = \theta_{c_{tip}} \quad 0.9 < r/R_t \leq 1$

Table 1. Rotor main geometric features

for wind tunnel wall effects, are determined. To estimate $Re^*_{0.7R}$, $Tu^*_{0.7R}$ and $k^*_{0.7R}$, the flow velocity relative to the blades is assumed to be composed of W^*_0 and solid body rotation only,

$$\begin{pmatrix} V^*_r \\ V^*_\theta \\ V^*_z \end{pmatrix} (r, \theta_b, z, \Psi, W^*_0) = \begin{pmatrix} W^*_0 sin\Psi sin\theta_b \\ W^*_0 sin\Psi cos\theta_b - \Omega r \\ W^*_0 cos\Psi \end{pmatrix}. \tag{2}$$

Using $|V^*| = \sqrt{(V^*_r)^2 + (V^*_\theta)^2 + (V^*_z)^2}$, $Re^*_{0.7R}$, $Tu^*_{0.7R}$ and $k^*_{0.7R}$ can be written as

$$Re^*_{0.7R} = \frac{c|V^*|}{\nu}, \tag{3}$$

$$Tu^*_{0.7R} = \sqrt{\frac{\bar{w^2}}{|V^*|^2}}, \tag{4}$$

$$k^*_{0.7R} = \frac{\omega c}{2\overline{|V^*|}}, \tag{5}$$

with c the airfoil chord, ν the kinematic viscosity and ω the frequency of phase-locked averaged inflow fluctuations present in yawed flow conditions, approximated by the 1P-harmonic, $\omega = \Omega$. $\overline{|V^*|}$ is the azimuthal average of $|V^*|$. $\bar{w^2}$ is a measure of the flow velocity fluctuations in the freestream direction, fluctuations in the other two directions are ignored. For nonzero Ψ, $|V^*|$ and correspondingly $Re^*_{0.7R}$ and $Tu^*_{0.7R}$ are a function of the blade azimuth angle θ_b. The thrust coefficient corrected for wind tunnel wall effects c^*_T, derived using the thrust T recorded with strain gauges placed on the rotor shaft for all three operating conditions [17], is given as

$$c^*_T = \frac{T}{\frac{1}{2}\rho W^*_0 \pi R^2_t}, \tag{6}$$

with ρ the air density. The three operating conditions are summarized in Table 2. In the remainder of the discussion, the indication * for wind tunnel wall corrected variables is omitted as only wind tunnel wall corrected variables are considered.

2.2. Tip Vortex Geometry

The centers of the tip vortices trailing the blades are localized by phase-locked quantitative smoke visualization [17]. The smoke patterns, recorded while a stroboscope illuminates the setup with the blades phase-locked at the $\theta_b = 90°$-position, are assumed to be located in the (x_m, z_m)-plane, see Figure 1 for the orientations. The average tip vortex location, determined from six recordings, is accompanied by an estimated random uncertainty $U_{x,z}$ at 95% confidence level of $U_{x,z} = 1 \cdot 10^{-2}$ m or $U_{x,z} = 2 \cdot 10^{-2} R_t$ for both the x_m- and z_m-direction. Measurements extend up to about $1R_t$ downstream and clearly indicate wake expansion and, for yawed flow, wake deflection towards the downwind side, see Figure 2.

Table 2. Flow conditions corresponding to the three experimental cases

	$W_0^*[m/s]$	$\lambda^*[-]$	$\theta_{c_{tip}}[^\circ]$	$k^*_{0.7R}[-]$	$Re^*_{0.7R} \cdot 10^{-5}[-]$		$Tu^*_{0.7R}[\%]$		$c_T^*[-]$
					max	min	max	min	
$\Psi = 0^\circ$	5.57	7.90	2.0°	-	1.65	-	0.39	-	0.77
$\Psi = 30^\circ$	5.47	8.05	2.0°	0.09	1.76	1.48	0.48	0.40	0.70
$\Psi = 45^\circ$	5.42	8.12	2.0°	0.09	1.79	1.40	0.38	0.48	0.52

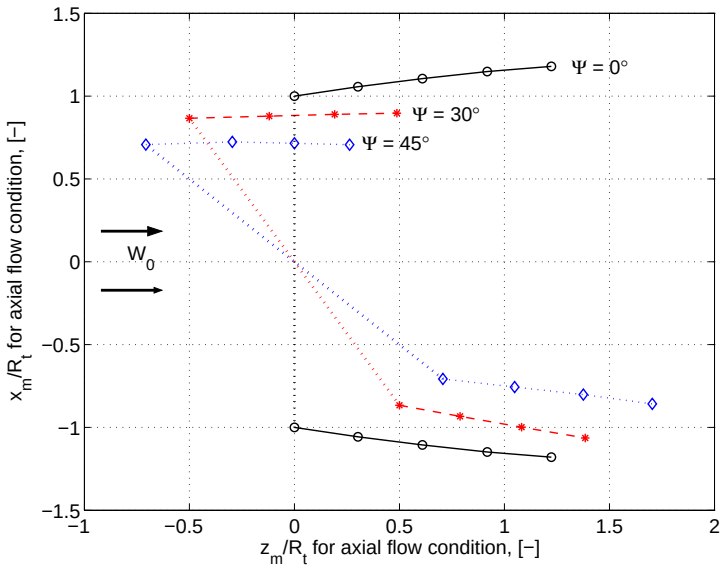

Figure 2. Average location of the tip vortex centers in the (x_m, z_m)-plane from quantitative smoke visualization with the blade positioned at $\theta_b = 90°$, for all three conditions. Tip vortex locations are expressed in the cartesian (x_m, z_m)-coordinates of the rotor in axial flow.

2.3. Phase Locked Average Velocity Distribution

The cyclic flow velocity field in the near-wake of the model rotor is reconstructed from phase-locked recordings of single sensor hot-films using a new data reduction technique [12, 18]. Tree downstream measurement planes are traversed, oriented parallel to the rotor plane and located at $z/R_t = 5.83 \cdot 10^{-2}$, $1.00 \cdot 10^{-1}$ and $1.50 \cdot 10^{-1}$. Phase-locked measurements are taken with an in-plane spatial resolution of $\Delta\theta = 15°$ and $\Delta(r/R_t) = 0.1$ in the azimuthal and radial direction, respectively. The blade azimuth resolution is $\Delta\theta_b = 2°$.

At a given spatial location, both the Phase-Locked Average (PLA) 'true' flow velocity vector $< \vec{V} >$ and the phase-locked standard deviation of the hot-film sensor output, the so-called effective velocity, s_{Veff}, are determined. The random uncertainty of $< \vec{V} >$ at a given (r, θ, z, θ_b)-point is separated into the velocity magnitude and velocity direction random uncertainty, $U_{|V|}$ and U_α, respectively. The uncertainty components at approximately 95% confidence level are estimated to be $U_{|V|} = 10\%$, relative to $| < \vec{V} > |$, and $U_\alpha = 5°$.

The near-wake distribution of the PLA velocity vectors reveals the unsteady three-dimensional flow field. The sample result for the $\Psi = 30°$ flow condition, given in Figure 3, clearly indicates the detail in the results and the non-axisymmetric nature of the flow. It can also be seen that s_{Veff} is a measure of the viscous wake passage.

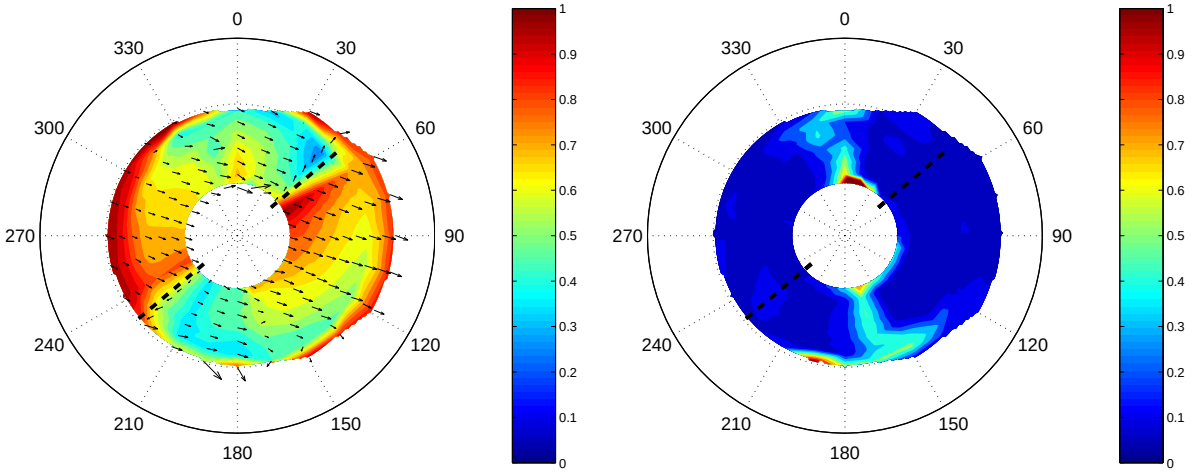

Figure 3. Hot-film measurement results at a plane $z/R_t = 5.83 \cdot 10^{-2}$ downstream for the $\Psi = 30°$ flow condition with blade orientation $\theta_b = 50°$. Viewpoint is upstream of the rotor, looking downstream, the blades rotate clockwise. Left plot: $<\vec{V}>$, with the contour indicating $V_z/(W_0 sin\Psi)$ and the vectors the in-plane velocity V_r and V_θ. Right plot: s_{Veff}.

3. Inverse vortex wake model

Both the concept and the construction of the first version of the inverse vortex wake model are discussed by Haans *et. al* [16]. At present, a summary of the model concept is given in Section 3.1, since the model concept for the updated version, discussed in this paper, is equal to that of the first version. The difference between the first and the updated version of the inverse vortex wake model concerns the discretization of the wake circulation, discussed in Section 3.2.

3.1. Model concept

The inverse vortex wake model is based on the assumption that the rotor flow field can be modeled by an incompressible, irrotational flow, with vortex singularities representing rotational flow at the blade and in the wake resulting from viscous effects. The velocity induced by such a three-dimensional vortex filament is given by the classical Biot-Savart law,

$$d\vec{v} = \frac{\Gamma}{4\pi}\left(\frac{d\vec{s}\times\vec{r}}{r^3}\right), \tag{7}$$

with $d\vec{s}$ an element of the vortex filament and $\vec{r}$ the distance between the point at which the induced velocity is determined and $d\vec{s}$.

The rotor flow field can be modeled by an incompressible, inviscid vortex system with bound circulation Γ_b on the blades and trailed and shed circulation in the wake, Γ_t and Γ_s, respectively. Conservation of circulation applies according to Kelvin's theorem

$$\frac{D\Gamma}{Dt} = 0. \tag{8}$$

Consequently, at time $t = t_1$ and blade position $r = r_1$, the bound circulation $\Gamma_b(r,t)$ is related to the circulation trailed and shed from the trailing edge at $r = r_1$, $d\Gamma_t(r_1,t_1)$ and $d\Gamma_s(r_1,t_1)$, respectively, with

$$d\Gamma_t(r_1,t_1) = -\left(\frac{\partial\Gamma_b(r,t)}{\partial r}\right)_{r_1,t_1} dr \tag{9}$$

and

$$d\Gamma_s(r_1,t_1) = -\left(\frac{\partial\Gamma_b(r,t)}{\partial t}\right)_{r_1,t_1} dt. \tag{10}$$

For yawed flow conditions, flow unsteadiness is assumed to be cyclic with the frequency equal to Ω. Time t can be replaced by the blade azimuth angle θ_b, with $\theta_b \,\epsilon\, [0°, 360°)$. Once trailed and shed into the wake, Γ_t and Γ_s are conserved. All the circulation in the vortex system can thus be expressed in terms of Γ_b.

The inverse vortex wake model is based upon two additional observations. First, the vortex wake location, orientation and convection velocity can be reconstructed from wake measurements. Second, substraction of $\vec{V_0} = (0, 0, W_0)$ from the PLA flow velocity $<\vec{V}>$, derived from measurements, yields the PLA induced flow velocity.

The known inducted velocity at given point (r, θ, z) and given θ_b can be expressed in terms of the unknown Γ_b by integration of the Biot-Savart equation [7] over all vortex filaments of the vortex wake system,

$$A(\Gamma_b) = <\vec{V}>(r, \theta, z, \theta_b) - \vec{V_0}, \tag{11}$$

with the general operator A acting on Γ_b. Solving Γ_b from equation [11] does not require an airfoil model/knowledge of the airfoil shape, contrary to prediction type vortex wake models.

The vortex wake system is discretized; each blade is represented by a single lifting line along which n filaments are taken and the rotational cycle is divided in m number of θ_b-intervals. For each filament i at each discrete cyclic instant $\theta_{b,j}$, $\Gamma_{b,i,j}$ is defined, with $i = 1, \ldots, n$ and $j = 1, \ldots, m$. For each discrete cyclic instant, p number of velocity components are determined at selected locations in the wake. Discretization of equation [11] yields

$$\begin{bmatrix} a_{1,1,1,1} & \cdots & a_{n,1,1,1} & \cdots & a_{1,m,1,1} & \cdots & a_{n,m,1,1} \\ \vdots & \ddots & \vdots & \cdots & \vdots & \ddots & \vdots \\ a_{1,1,1,p} & \cdots & a_{n,1,1,p} & \cdots & a_{1,m,1,p} & \cdots & a_{n,m,1,p} \\ \vdots & \vdots & \vdots & \vdots & \vdots & \vdots & \vdots \\ \vdots & \vdots & \vdots & \vdots & \vdots & \vdots & \vdots \\ a_{1,1,m,1} & \cdots & a_{n,1,m,1} & \cdots & a_{1,m,m,1} & \cdots & a_{n,m,m,1} \\ \vdots & \ddots & \vdots & \cdots & \vdots & \ddots & \vdots \\ a_{1,1,m,p} & \cdots & a_{n,1,m,p} & \cdots & a_{1,m,m,p} & \cdots & a_{n,m,m,p} \end{bmatrix} \begin{bmatrix} \Gamma_{b,1,1} \\ \vdots \\ \Gamma_{b,n,1} \\ \vdots \\ \Gamma_{b,1,m} \\ \vdots \\ \Gamma_{b,n,m} \end{bmatrix} = \begin{bmatrix} <V_{1,1}> \\ \vdots \\ <V_{1,p}> \\ \vdots \\ \vdots \\ <V_{m,1}> \\ \vdots \\ <V_{m,p}> \end{bmatrix} - \vec{V_0}. \tag{12}$$

The influence matrix size is $(p*m)\times(n*m)$. Its indices $a_{i,j,k,l}$ indicate: circulation related to the bound circulation at blade filament i $(i = 1, \ldots, n)$ for blade azimuth angle $\theta_{b,j}$ $(j = 1, \ldots, m)$, equation set up for blade azimuth angle $\theta_{b,k}$ $(k = 1, \ldots, m)$ and for velocity component l $(l = 1, \ldots, p)$. An overdetermined system, hence with $p > n$, is set up to reduce the sensitivity of the system to a particular measurement. A solution to system of equations [12] is obtained with the Least-Squares method.

3.2. Model construction

In order to set up system of equations [12], a discretized vortex wake geometry should be reconstructed from the near-wake measurements, the circulation on each wake element should be expressed in terms of Γ_b and points should be selected at which the measured velocity is compared with computed velocity. Although the construction of the updated model mostly overlaps with that of the first version in [16], a discussion is presented in this section to obtain an integral overview of the updated model, thereby avoiding confusion as to what are the (dis)similarities between the two versions of the inverse vortex wake model.

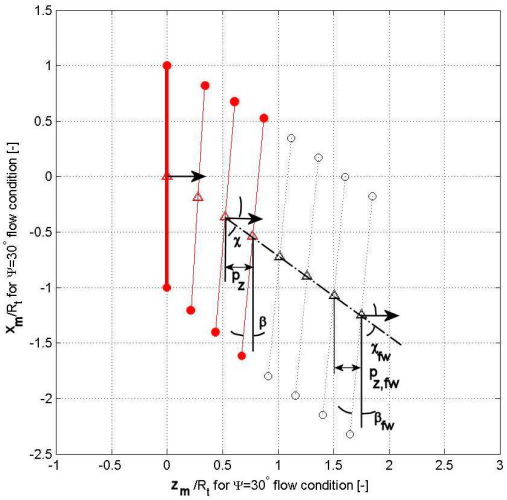

Figure 4. Tip vortices in the (x_m, z_m)-plane for the $\Psi = 30°$ condition. Closed symbols, solid line: measurements. Open symbols, dotted lines: estimates. Induced velocity in the far wake is assumed uniform and derived from the measurements furthest downstream. Consequently, wake skew angle $\chi = \chi_{fw}$, wake twist angle $\beta = \beta_{fw}$ and z_m-pitch $p_z = p_{z,fw}$.

3.2.1. Discretized wake geometry & circulation Near-wake measurements form the basis of a discretized reconstruction of the vortex wake geometry. Three parts can be identified;

- a very-near-wake, up to $z/R_t \approx 1.50 \cdot 10^{-1}$, containing measured tip vortex paths, estimated root vortex paths and measured vortex sheet paths
- a near-wake, up to about $z/R_t = 1$, containing measured tip vortex paths and estimated root vortex paths
- far-wake, containing estimated tip and root vortex paths

The vortex sheet paths in the very-near-wake are found using both $< \vec{V} >$- and s_{Veff}-data. Measured s_{Veff}-distributions yield viscous wake locations, see e.g. Figure 3. Measured $< \vec{V} >$-distributions at the identified viscous wake locations then lead to the viscous wake convection velocity vector.

The tip vortex paths in the very-near-wake and the near-wake are reconstructed from measured tip vortex center locations, see Figure 2; lines are drawn in the (x_m, z_m)-plane that connect vortex centers on the upstream and downstream side with identical wake age, see Figure 4. Circles are constructed in the planes defined by these lines and lines parallel to the y_m-axis. The circle centers coincide with the midpoints of the lines connecting two vortex centers and the circle diameters are equal to the lengths of the lines connecting two vortex centers. The circles yield the outline for the helical tip vortex paths that are assumed to trail from the blade tip, $r = R_t$.

No tip vortex measurements are available in the far-wake, starting at $z/R_t \approx 1$. The tip vortex path geometry is estimated by assuming that the tip vortex convection velocity is constant and equal to the convection velocity of the 'tip vortex circle' center in the measurement plane furthest downstream. Consequently, the far-wake tip vortex paths do not expand.

The construction of the root vortex paths is based on assumptions only, since no root vortex measurements are performed. It is assumed that the root vortices trail the blade at the root, $r = R_r$, and that the root vortex paths do not expand. The root vortex convection velocity

The vortex sheet trailed behind a rotor blade rolls up into a concentrated tip and root vortex. The circulation of the concentrated tip and root vortices after roll-up equals the summation of the circulation over all trailed vortex elements rolling up to form the tip and root vortices, respectively. Circulation hence is conserved. The concentrated tip and root vortices after roll-up generally are of equal strength and opposite sign, with strength equal to the bound circulation maximum $\Gamma_{b,max}$.

In the inverse vortex wake model, vortex sheet roll-up into the tip and root vortices is imposed a priori; roll-up is prescribed at the boundary between the very-near-wake and the near-wake and a blade spanwise location r_s is preselected where the most outboard vortex element rolling up into the root vortex trails the blade.

Concentrated tip and root vortices after roll-up of the same strength, equal to $\Gamma_{b_{max}}$, and opposite sign are found when r_s corresponds to the computed spanwise location of $\Gamma_{b_{max}}$. Hence, a posteriori, r_s is compared to the r-location of $\Gamma_{b,max}$ for the computed Γ_b-distribution. If required, a new location is selected.

The vortex wake is discretized with linear, constant circulation strength vortex filaments, using a spatial resolution of $\Delta(r/R_t) = 0.1$ for vortex filament nodes on the lifting line and a cyclic resolution of $\Delta\theta_b = 15°$. The notation of the vortex filaments is introduced in the left plot of Figure 5. Bound circulation is denoted as $\Gamma_{b,i,j}$. At given $\theta_b = \theta_{b,k}$, $(\Gamma_{b,i,j})_{j=k}$ represents the actual bound circulation on the blade filaments, trailing and shed circulation filaments are ordered with $\Gamma_{t,i,k,l}$ and $\Gamma_{s,i,k,l}$, respectively, with suffix l indicating the filament wake age, $l = 1$ at the time of trailing/shedding.

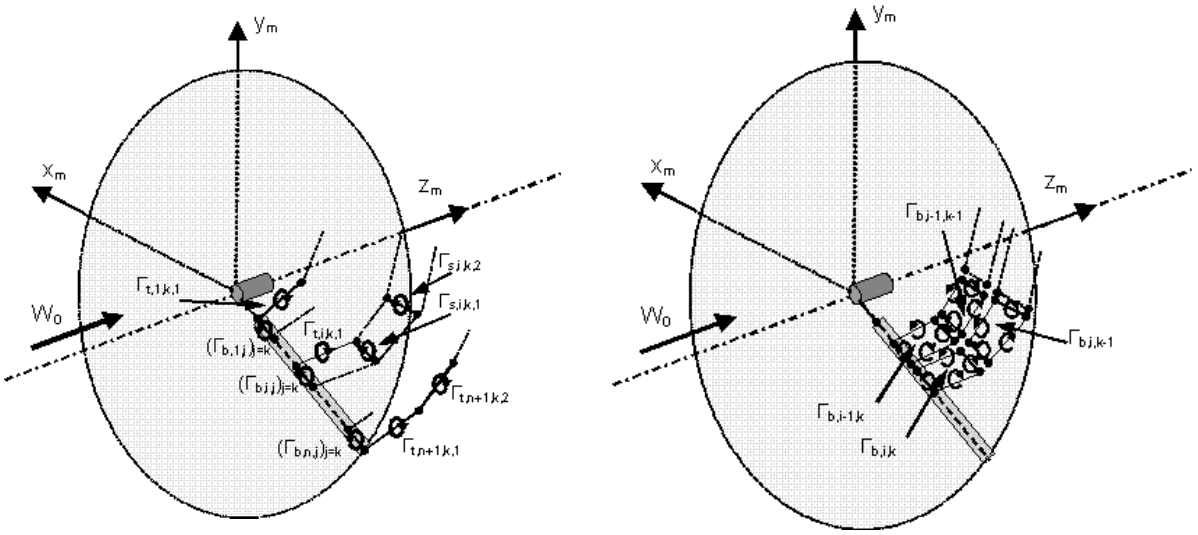

Figure 5. Schematic of the discretized wake circulation for the blade at $\theta_{b,k}$. Left plot: notations, right plot: vortex ring concept.

Circulation is conserved by applying constant strength closed vortex rings, see the right plot of Figure 5. Discretization of equations [9] and [10] hence yields

$$\Gamma_{t,i,k,1} = -(\Gamma_{b,i,j} - \Gamma_{b,i-1,j})|_{j=k} \tag{13}$$

and

$$\Gamma_{s,i,k,1} = -(\Gamma_{b,i,j} - \Gamma_{b,i,j-1})|_{j=k}. \tag{14}$$

The vortex wake system is hence analyzed at discrete cyclic instants $\theta_{b,k}$. At given $\theta_{b,k}$, the vortex filaments shed from the trailing edge between $\theta_{b,k-1}$ and $\theta_{b,k}$ have a wake age of $0.25\Delta\theta_b$,

in accordance with the suggestion by Katz and Plotkin [20], in order to obtain an appropriate contribution to the induced velocity at the lifting line from shed vorticity. Note that the vortex filaments are shed from the trailing edge, located $3/4c$ from the lifting line. For given $\theta_{b,k}$, the θ-coordinate of the trailing edge is approximately

$$\theta_{TE} = \theta_{b,k} - \frac{3/4c}{2\pi r} 360^\circ. \tag{15}$$

3.2.2. Velocity points selection Discussions by Vermeer [14] and Mast *et al.*[15] aid in the selection of (r, θ, z, θ_b)-points at which the induced velocity is reconstructed.

Vermeer [14] observes that a system of equations computing a spanwise bound Γ_b-distribution from near-wake velocity measurements becomes ill-conditioned when the velocity points are selected at a single radial position r_1 only. The induced velocity at r_1 in the near-wake is dominated by $\Gamma_b(r_1)$, contributions diminish for bound vortex filaments positioned away from r_1. Vermeer's analysis model considers the contribution of bound circulation only to induced velocity. In essence however the present, more extensive, inverse vortex wake model also requires velocity points at r-stations all along the blade for a well-conditioned system of equations. Velocity points are selected accordingly.

Mast *et al.*[15] show that a lifting line model does not accurately predict the induced velocity at a velocity point in close proximity to a passing blade. The lifting line model under-predicts the local induced velocity minima and maxima associated with a blade passage. The difference between measurements and modeling results is attributed to the displacement effect, the influence of distributed vorticity along the airfoil contour on the induced velocity, that is missing in the lifting line modeling. The selected velocity points thus are positioned away from the local induced velocity maxima and minima of a blade passage at $\theta \approx \theta_b$.

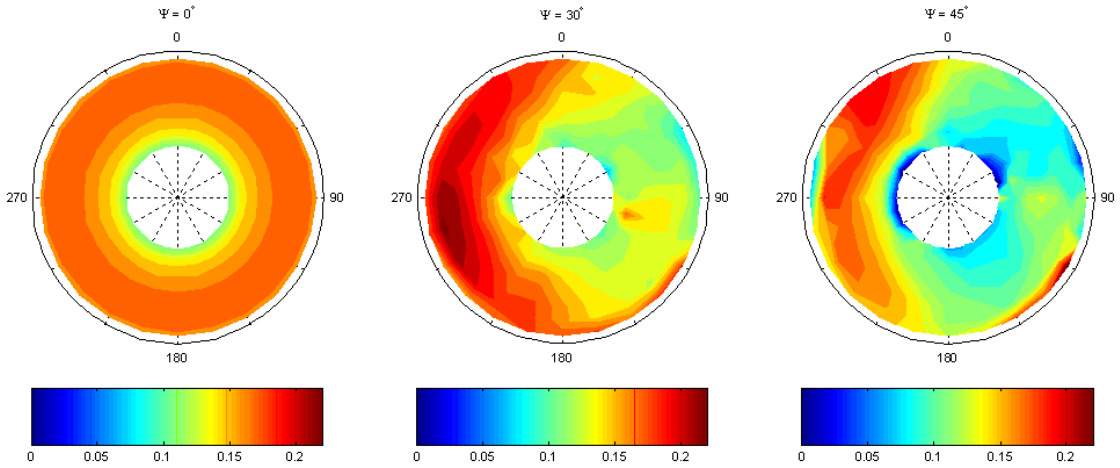

Figure 6. $\Gamma_b/(W_0 R_t)$-distribution at the lifting line during a blade cycle, plotted as a $\Gamma_b/(W_0 R_t)$-contour in the rotor plane. Left plot: $\Psi = 0^\circ$, middle plot: $\Psi = 30^\circ$, right plot: $\Psi = 45^\circ$.

4. Results

Inverse vortex wake model settings for the results shown are bound circulation filament end-node location at $r/R_t = 0.3, 0.4, \cdots 1.0$, hence $\Delta r/R_t = 0.1$, and cyclic resolution $\Delta\theta_b = 15^\circ$. Furthermore, the root and tip vortices are assumed to trail at R_r and R_t, respectively. $r_s/R_t = 0.8$ is selected for all three cases.

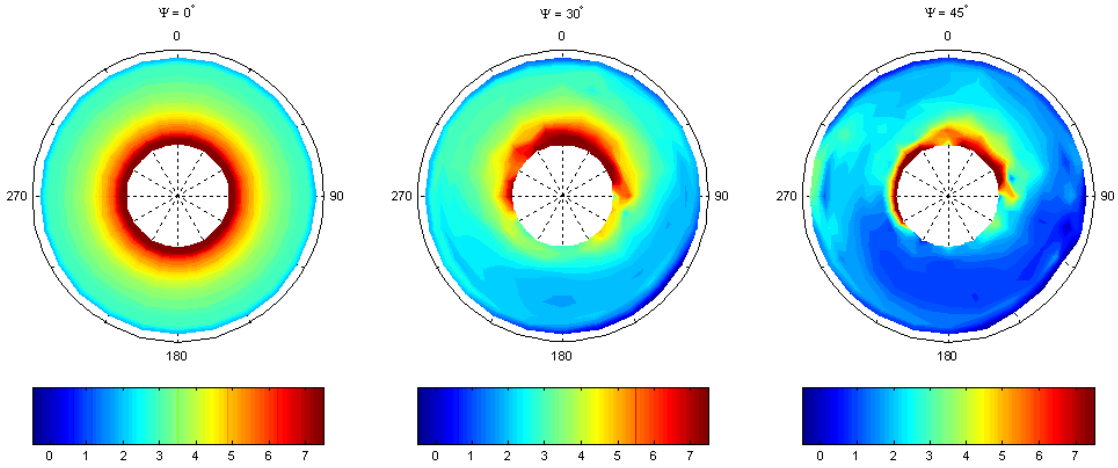

Figure 7. α-distribution at the lifting line during a blade cycle, plotted as a α-contour in the rotor plane.

4.1. Experimental conditions at the lifting line

Having computed the cyclic spanwise Γ_b-distribution with the inverse vortex wake method, see Figure 6, the wake vortex system is fully determined; the position, orientation and circulation of each vortex filament are known. The inflow can hence be reconstructed, including the angle of attack α-distribution, see Figure 7. With known inflow and Γ_b-distribution, the blade lift L is determined from the Kutta-Joukowski law,

$$L = \rho \vec{V} \times \vec{\Gamma}_b, \tag{16}$$

with L the lift per unit span and $\vec{V}$ the flow velocity at the lifting line, relative to the rotating blade. Correspondingly, the lift coefficient c_l can be expressed as

$$c_l = \frac{2\Gamma_b}{cV}, \tag{17}$$

with c the blade chord length. See Figure 8 for the c_l-distribution. Note that no airfoil model is needed to determine c_l.

The plots of the spanwise Γ_b-, α- and c_l-distributions at the lifting line during a blade cycle, given in Figures 6 to **??**, confirm that the aerodynamics of a rotor subject to a nonzero yaw angle Ψ are characterized by periodically unsteady blade flow conditions and a non-axisymmetric wake. The general trends seen for $\Psi = 30°$ recur for $\Psi = 45°$.

Wind tunnel measurements on the NACA0012 airfoil yield stalls at $\alpha_{stall} = 10.6°$ for $Re = 1.5 \cdot 10^5$, which is within the range of Re-numbers for the near-wake rotor measurements. For all operating conditions, $\alpha < \alpha_{stall}$ generally holds, see Figure 7. It can be assumed that the yawed flow conditions do not result in substantial regions of dynamic stall on the blades. The absence of dynamic stall should reduce the complexity of the inflow distribution in the rotor plane.

4.2. Contributions to the inflow at the rotor plane

The inflow at the rotor plane is analyzed using three velocity variables

- Annular averaged velocity $\overline{\vec{V}}_{ann}$: the average of the velocity in the annular circle with radius r/R_t and distance z/R_t from the rotor plane for given blade orientation θ_b

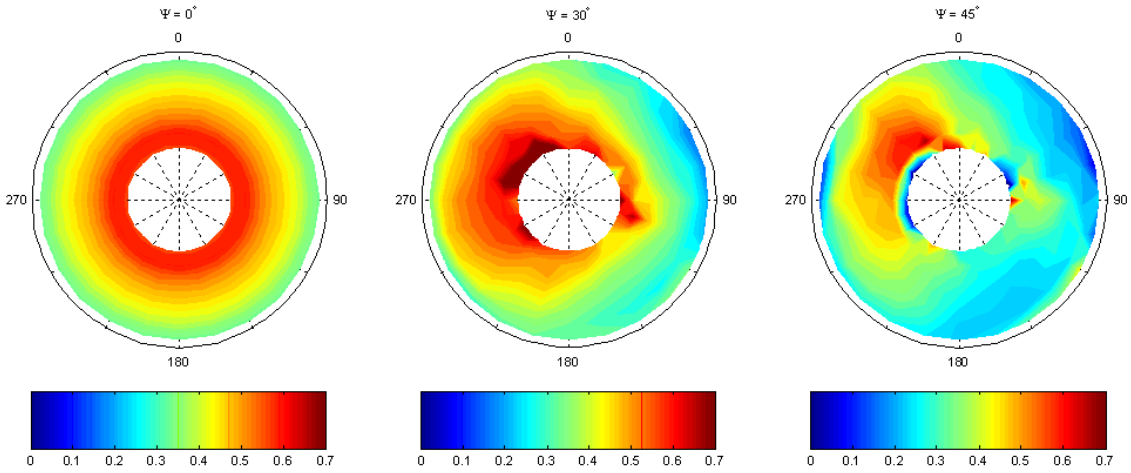

Figure 8. c_l-distribution at the lifting line during a blade cycle, plotted as a c_l-contour in the rotor plane.

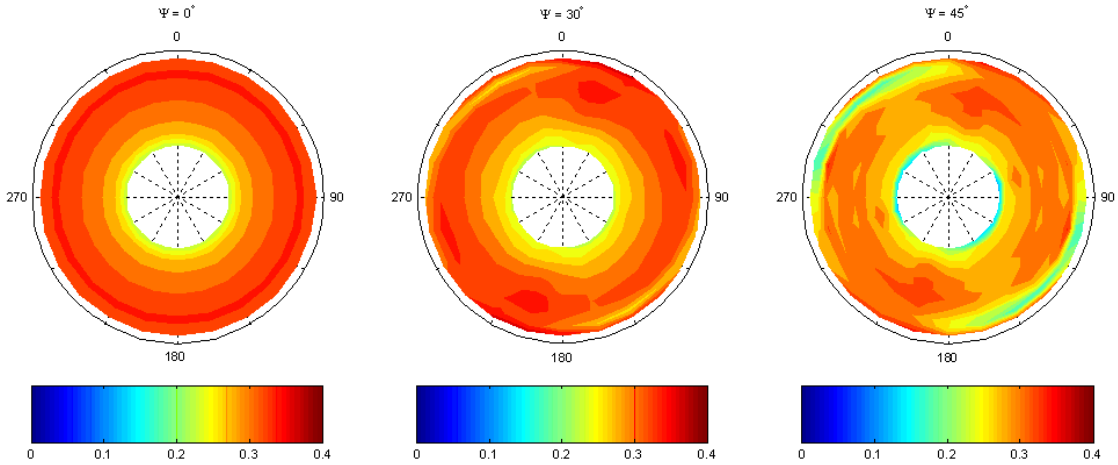

Figure 9. $[1 - \overline{V_{zann}}/(W_0 cos\Psi)]$-distribution in the rotor plane. The contour represents the $[1 - \overline{V_{zann}}/(W_0 cos\Psi)]$-value for the annulus with radius r/R_t at cyclic instant θ_b.

- Cycle averaged velocity $\overline{\vec{V}}_{cyc}$: the average of the velocity at given wake location $(r/R_t, \theta, z/R_t)$ over a full blade cycle
- Lifting line velocity $\vec{V}$: the velocity at given spanwise position r/R_t on the lifting line

The study of $\overline{\vec{V}}_{ann}$ is relevant for BEM-based rotor aerodynamic codes. A BEM-based method computes the equilibrium between the Momentum part, formulated using the annular averaged axial velocity $\overline{V_{zann}}$ at the rotor plane, and the Blade Element part at each annulus.

The $\overline{V_{zann}}$-distribution in the rotor plane, shown in Figure 9, appears to be nearly axisymmetric, for both the axial and the yawed flow conditions. Asymmetric contributions resulting from yaw misalignment are minor. Hence at a given radial coordinate r/R_t, $\overline{V_{zann}}$ is quasi-steady during a blade cycle. For $\Psi = 45°$, the unsteadiness increases compared to $\Psi = 0°, 30°$.

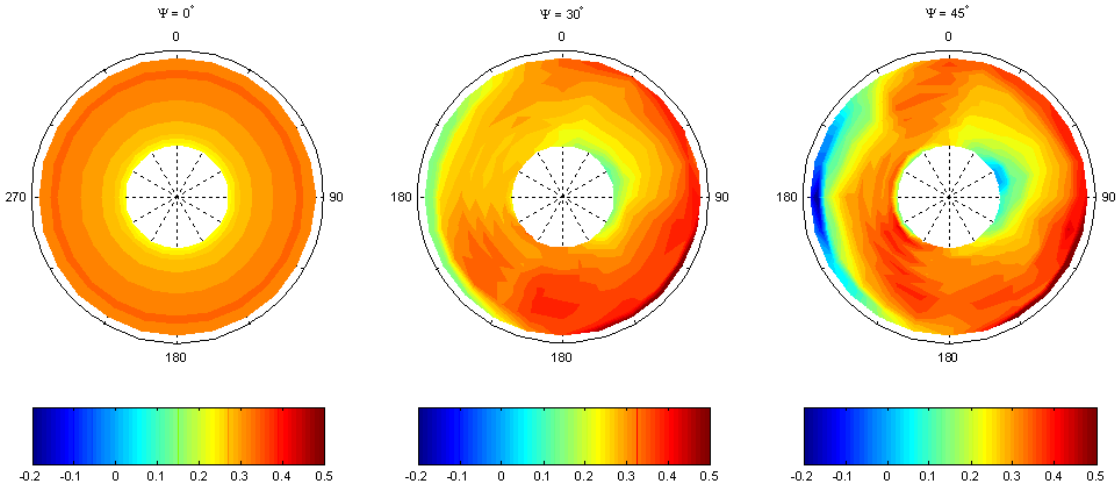

Figure 10. Contour of $[1 - \overline{V_{zcyc}}/(W_0 cos\Psi)]$ in the rotor plane.

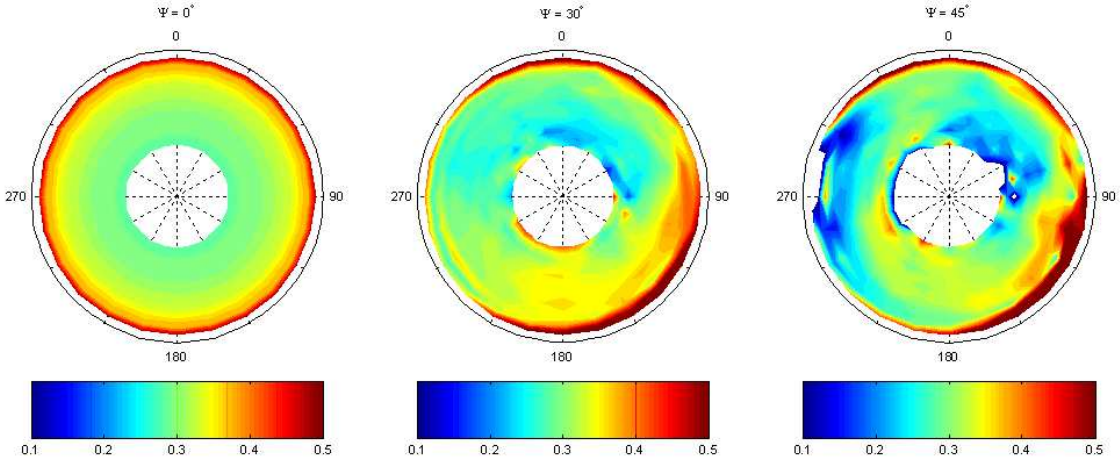

Figure 11. $[1 - V_z/(W_0 cos\Psi)]$-distribution at the lifting line during a blade cycle, plotted as a $[1 - V_z/(W_0 cos\Psi)]$-contour in the rotor plane.

The inflow asymmetry introduced by yaw misalignment can clearly be seen by the cycle averaged axial velocity $\overline{V_{zcyc}}$-distribution, shown in Figure 10. The asymmetric $\overline{V_{zcyc}}$-distribution indicates that the induced velocity at a blade section varies during the rotational cycle, contrary to the observation from the $\overline{V_{zann}}$-distribution. The annular averaged inflow computed by BEM-based methods is hence generally corrected to account for the unsteadiness resulting from yawed flow. Schepers [21] suggests an inflow correction model based on $\overline{V_{zcyc}}$-measurements.

The trends in the axial velocity at the lifting line V_z and $\overline{V_{zcyc}}$ agree, compare Figure 10 with 11, respectively. The smoother contours for $\overline{V_{zcyc}}$ result from cycle averaging. The discussion on the phenomena governing the inflow in the rotor plane is illustrated with V_z-contour plots, see Figures 12 to 15, but holds for $\overline{V_{zcyc}}$ too. Note that the range for the dimensionless is set to 0.5 for each plot, enabling mutual comparison.

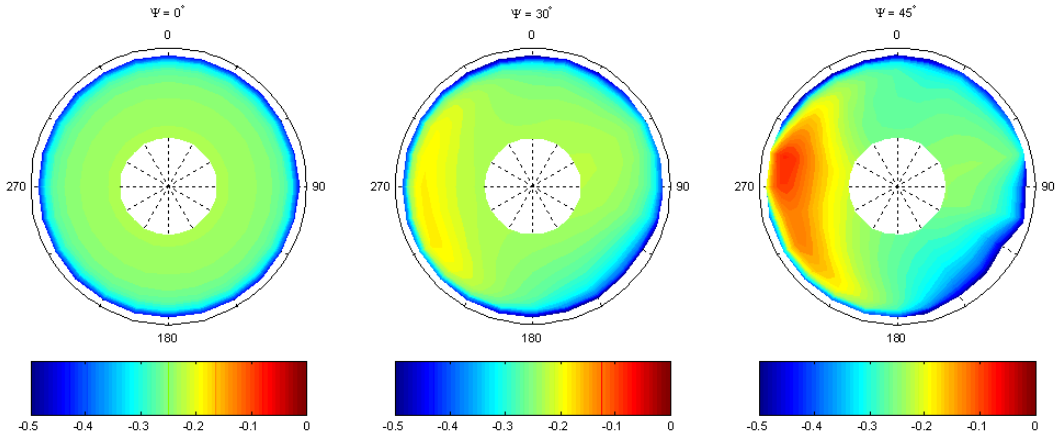

Figure 12. Tip vortex contribution to $V_z/(W_0 cos\Psi)$ at the lifting line during a blade cycle, plotted as a $V_z/(W_0 cos\Psi)$-contour in the rotor plane.

The contribution of the tip vortices to the induced velocity shows a distinct pattern of increasingly negative V_z, hence oriented upstream, when going from the upwind to the downwind side of the rotor plane, see Figure 2. The non-axisymmetric downstream convection of the tip vortices in yaw leads to a smaller average distance between a blade section and tip vortices for the blade on the upwind than on the downwind side. Consequently, the magnitude of V_z induced by the tip vortices is higher on the upwind than on the downwind side. This phenomenon is approximated by the sinusoidal-type Glauert inflow correction model [22].

The root vortices clearly induce positive V_z, hence oriented downstream, on the inboard sections of the blade when it passes through the downwind region, see Figure 13. The inverse vortex wake model hence qualitatively agrees with numerical studies by e.g. Snel [23] that acknowledge the skewed root vortex effect. Note that increased V_z on the inboard sections with the blade positioned in downstream direction results in a destabilizing contribution to the yawing moment. A secondary effect is negative V_z induced by the root vortex for the blade in the advancing region.

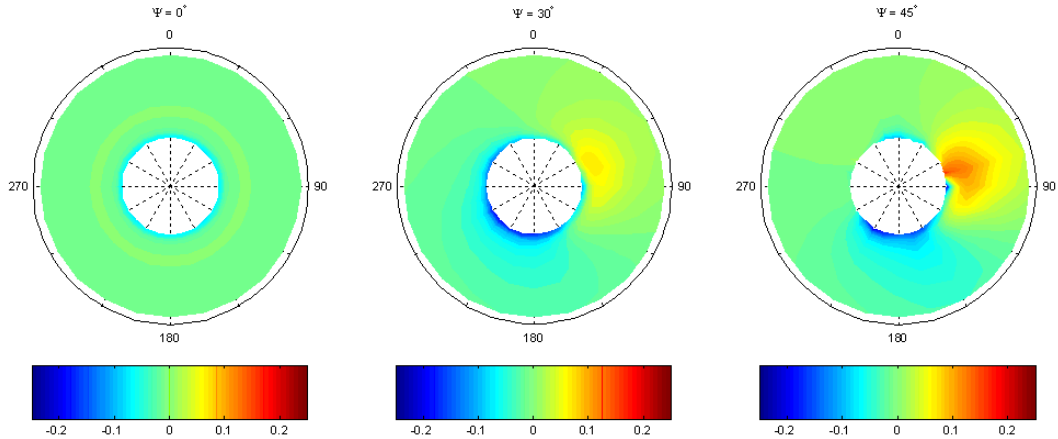

Figure 13. Root vortex contribution to $V_z/(W_0 cos\Psi)$ at the lifting line during a blade cycle, plotted as a $V_z/(W_0 cos\Psi)$-contour in the rotor plane.

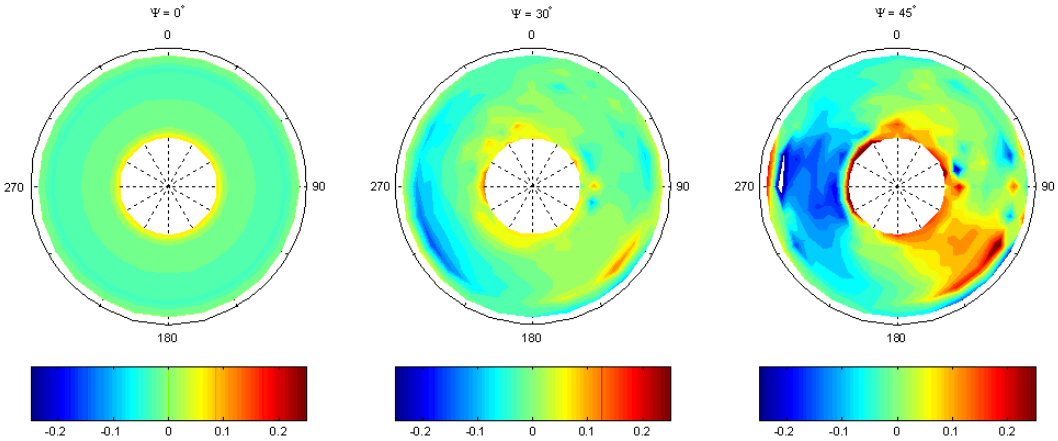

Figure 14. Trailed vortex sheet contribution to $V_z/(W_0 cos\Psi)$ at the lifting line during a blade cycle, plotted as a $V_z/(W_0 cos\Psi)$-contour in the rotor plane.

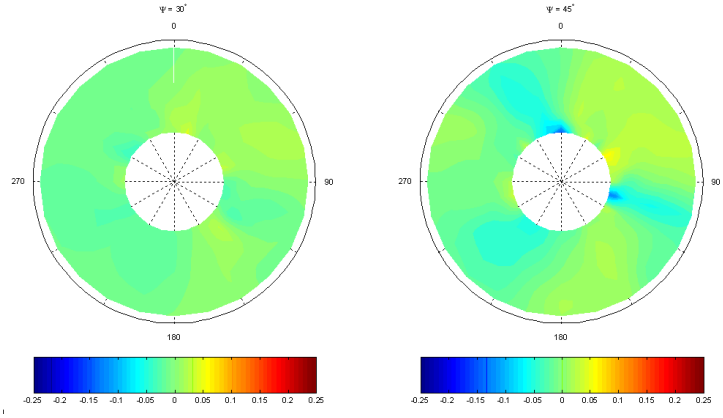

Figure 15. Shed vortex sheet contribution to $V_z/(W_0 cos\Psi)$ at the lifting line during a blade cycle, plotted as a $V_z/(W_0 cos\Psi)$-contour in the rotor plane.

With the rotor operating in yaw misalignment, the trailed wake circulation does yield a substantial contribution to the induced velocity V_z at the lifting line, whereas the effect of the shed wake circulation is insignificant, compare Figures 14 and 15. For the present yawed flow operating conditions, the shed wake circulation contribution to the inflow can hence be ignored.

5. Conclusions

Near-wake measurements are conducted on a wind turbine rotor model in an open jet wind tunnel. The focus is on yawed flow conditions, whilst a baseline axial flow condition is recorded as well. Tip vortex center locations and phase-locked average flow velocity distributions are measured.

Measurements are not available in the rotor plane and detailed blade loads are not recorded. The blade conditions hence are not directly available from the experiments. In order to estimate the experimental blade conditions, an analysis model is constructed. The method is based on conservation of circulation in the vortex wake system, consisting of bound circulation on the

blades and trailed and shed circulation in the wake. The approach is named 'inverse vortex wake method', where inverse suggests that the tool is used to analyze wake measurements instead of predicting blade conditions from a rotor geometry and operating condition only.

Derived spanwise distributions of the bound circulation, angle of attack and lift coefficient as a function of the blade azimuth angle reveal unsteady, attached blade conditions. The annular averaged inflow appears to be quasi-axisymmetric, whilst cycle averaged inflow and the velocity at the lifting line are asymmetric.

The inverse vortex wake model allows assessment of the individual contributions of tip, root, trailed and shed vortices to the inflow in the rotor plane. Found tip and root effects correlate well with those reported in literature. For the conditions studied, shed vortex contributions can be ignored.

Acknowledgments
Simon Toet and Kees van Beek, both from TUDelft, are kindly acknowledged by the authors for their assistance and trouble shooting during the experiments. Tonio Sant, who obtained a PhD from TUDelft and currently works at the University of Malta, is thanked for his contributions to the execution and analysis of the measurements.

[1] M.O.L. Hansen, J.N. Sørensen, S. Voutsinas, N. Sørensen, and H.Aa. Madsen. State of the art in wind turbine aerodynamics and aeroelasticity. *Progress in aerospace sciences*, 42:285–330, 2006.
[2] D. Simms, S. Schreck, M. Hand, and L.J. Fingersh. Nrel unsteady aerodynamics experiment in the nasa-ames wind tunnel: A comparison of predictions to measurements. Technical Report NREL/TP-500-29494, NREL, Boulder, Colorado.
[3] J.G. Leishman. Challenges in modelling the unsteady aerodynamics of wind turbines. *Wind Energy*, 5:85–132, april-september 2002.
[4] H. Snel. Review of the present status of rotor aerodynamics. *Wind Energy*, 1:46–69, april 1998.
[5] H. Snel. Review of aerodynamics for wind turbines. *Wind Energy*, 6, Issue 3:203–211, July/September 2003.
[6] L.J. Vermeer, J.N. Sørensen, and A. Crespo. Wind turbine wake aerodynamics. *Progress in Aerospace Sciences*, 39/6-7:467–510, August-October 2003.
[7] W.Z. Shen, M.O.L. Hansen, and J.N. Sørensen. Determination of angle of attack (aoa) for rotating blades. In *EUROMECH Colloquium 464b Wind Energy*, Oldenburg, Germany.
[8] R.P.J.O.M. van Rooij, W.A. Timmer, and A. Bruining. Determination of the local inflow angle on rotating blades. In *Proceedings of the World Wind Energy Conference and Exhibition*, Berlin, Germany, July 2002.
[9] J.L. Tangler. Insight into wind turbine stall and post-stall aerodynamics. *Wind Energy*, 7:247–260, 2004.
[10] T. Sant, G.A.M. van Kuik, and G.J.W. van Bussel. Estimating the angle of attack from blade pressure measurements on the nrel phase vi rotor using a free wake vortex model: axial conditions. *Wind Energy*, Vol. 9, No. 6:549–577, November/December 2006.
[11] M.O.L. Hansen, N.N. Sørensen, J.N. Sørensen, and J.A. Michelsen. Extraction of lift, drag and angle of attack from computed 3-d viscous flow around a rotating blade. In *EWEC 1997*, pages 499–501, Dublin, Ireland, October 1997.
[12] W. Haans, T. Sant, G.A.M. van Kuik, and G.J.W. van Bussel. Hawt near wake aerodynamics, part i: Axial flow conditions. *Wind Energy*, Under review:Under review, Under review.
[13] N-J. Vermeer and G.J.W. van Bussel. Velocity measurements in the near wake of a model rotor and comparison with theoretical results. In *1990 European Community Wind Energy Conference Proceedings*, pages 218–222, Madrid, Spain, September 1990.
[14] N-J Vermeer. Local circulation on rotating wind turbine blades from velocity measurements in the wake of a model rotor. In *Proceedings of the 14th British Wind Energy Association Conference*, Nottingham, England.
[15] E.H.M. Mast, L.J. Vermeer, and G.J.W. van Bussel. Estimation of the circulation distribution on a rotor blade from detailed near wake velocities. *Wind Energy*, Vol. 7, No. 3:189–209, July/September 2004.
[16] W. Haans, G.A.M. van Kuik, and G.J.W. van Bussel. The inverse vortex wake model: a measurement analysis tool, aiaa-2007-0422. In *26th ASME Wind Energy Symposium, 45th AIAA Aerospace Sciences Meeting and Exhibit*, Reno, Nevada, January 2007.
[17] W. Haans, T. Sant, G.A.M. van Kuik, and G.J.W. van Bussel. Measurement of tip vortex paths in the wake of a hawt under yawed flow conditions. *Journal of Solar Energy Engineering*, Vol. 127, No. 4:456–463, November 2005.
[18] W. Haans, T. Sant, G.A.M. van Kuik, and G.J.W. van Bussel. Velocity measurements in the near wake

of a horizontal axis wind turbine. In *31st European Rotorcraft Forum*, pages 61.1–61.14, Florence, Italy, September 2005.

[19] W. Haans, T. Sant, G.A.M. van Kuik, and G.J.W. van Bussel. Stall in yawed flow conditions: A correlation of blade element momentum predictions with experiments. *Journal of Solar Energy Engineering*, Vol. 128, No. 4:472–480, November 2006.

[20] J. Katz and A. Plotkin. *Low-Speed Aerodynamics*. Cambridge University Press, Cambridge, England, 2001.

[21] J.G. Schepers. An engineering model for yawed conditions, developed on basis of wind tunnel measurements. *AIAA-paper*, 1999-0039:164–174, 1999.

[22] H. Glauert. A general theory for the autogyro. Technical Report ARC R & M 786, ARC, 1926.

[23] H. Snel. Survey of induction dynamics modelling within bem-like codes: dynamic inflow and yawed flow modelling revisited, aiaa-2001-0027. In *20th ASME Wind Energy Symposium, 39th AIAA Aerospace Sciences Meeting and Exhibit*, Reno, Nevada, January 2001.